A Numerical Study of The Heat Transfer Intensification Using High Amplitude Acoustic Waves

Sebastian RULIK, Włodzimierz WRÓBLEWSKI

Institute of Power Engineering and Turbomachinery
Silesian University of Technology
Konarskiego 18, 44-100 Gliwice, Poland; e-mail: {sebastian.rulik, wlodzimierz.wroblewski}@polsl.pl

The current practice in the efforts aiming to improve cooling conditions is to place emphasis on the application of non-stationary flow effects, such as the unsteady jet heat transfer or the heat transfer intensification by means of a high-amplitude oscillatory motion. The research presented in this paper follows this direction.

A new concept is put forward to intensify the heat transfer in the cooling channels with the use of an acoustic wave generator. The acoustic wave is generated by a properly shaped fixed cavity or group of cavities.

The sound generated by the cavity is a phenomenon analysed in various publications focused on the methods of its reduction. The phenomenon is related to the feedback mechanism between the vortices flowing from the leading edge and the acoustic waves generated within the cavity. The acoustic waves are generated by the interaction between the vortices and the cavity walls. Strong instabilities can be observed within a certain range of the free flow velocities. The investigations presented in this paper are oriented towards the use of the phenomenon for the purposes of the heat transfer process intensification.

The first part of the work presents the numerical model used in the analysis, as well as its validation and comparison with empirical relations. The numerical model is constructed using the commercial CFD Ansys CFX-16.0 commercial program.

The next part includes determining of the relationship between the amplitude of the acoustic oscillations and the cooling conditions within the cavity. The calculations are performed for various flow conditions.

Keywords: cavity noise; sound wave cooling; flow over a cavity; transient cooling; blade cooling intensification.

Nomenclature

A – surface area of the cavity neck cross-section [m^2],
c – sound velocity [m/s],
f – frequency [Hz],
HTC – heat transfer coefficient [W/(m^2·K)],
k – ratio between the vortex convection and the free flow velocity [–],
k_e – turbulence kinetic energy [J/kg],
m – mode number [–],
m_x – cavity mode in direction x [–],
m_y – cavity mode in direction y [–],
m_z – cavity mode in direction z [–],
M – Mach number [–],
u – velocity [m/s],
L – cavity or cavity neck length [m],
D – cavity depth [m],
W – cavity width [m],

h – specific enthalpy [kJ/kg],
p – pressure [Pa],
r_c – recovery factor [–],
t – time [s],
T – temperature [K],
V – cavity volume [m^3],
Z – cavity neck height [m],

Greek symbols

λ – wave length [m],
α – phase shift between vortices [–],
μ – dynamic viscosity [Pa·s],
κ – specific heat ratio [–],
ω – turbulence frequency [1/s],
$\boldsymbol{\tau}$ – shear stress tensor [kPa],
$\mathbf{I}$ – identity tensor [–],

Subscripts

w – vortex [–],
wall – walls [–],
ad – adiabatic [–],
a – sound [–],
∞ – free flow [–],
c – convection [–],
t – turbulent,
tot – total [–],
eff – effective [–].

1. Introduction

The turbulence arising in the fluid flow generates acoustic waves. Their presence may cause unfavourable effects, such as noise, but the waves can also be used in synergy with other phenomena to amplify their effect. The item which is often taken up in literature as a source of the acoustic wave is the cavity located transversely to the fluid flow direction. The acoustic wave generated in such circumstances is emitted to the environment and perceived as noise, which – in some conditions – is also accompanied by high-amplitude pressure pulsations in the cavity. Although fairly extensive research has already been conducted on the issue, the phenomenon still remains the subject of many numerical and experimental studies aiming to reduce the level of noise emission. This is of special importance in the aircraft and automotive industries. A typical example here is the noise generated by the aircraft open undercarriage or bomb hatch or by the gap between the car door and body (ASHCROFT *et al.*, 2000; HENDERSON, 2000; LOH, 2004). Numerical and experimental studies usually take account of the flow conditions and of the cavity geometries corresponding to the cases mentioned above.

The aim of the investigations presented in this paper is to analyse the impact of the acoustic wave generated in the cavity on the heat transfer intensification. Using a non-stationary phenomenon in the form of an acoustic wave to improve the heat transfer process is a part of the general trend of developing new cooling techniques needed in different industries. Active methods are an interesting example of the techniques applied in this area. In them, the heat transfer is intensified by means of periodic changes in the motion of the walls that affect the flow. The techniques include as follows (LÉAL *et al.*, 2013):

- using a high-amplitude acoustic wave (ultrasound) generated by a diaphragm,
- using a synthetic jet, where the flow is forced by the motion of a diaphragm placed in the cavity,
- elastic deformation or the wall high-amplitude motion.

A survey of cooling techniques based on the use of ultrasound is made by LEGAY *et al.* (2011). Attention is drawn in this case to several key effects related to propagation of a high-frequency acoustic wave in a liquid. One of them is the acoustic cavitation mechanism which improves the heat transfer conditions substantially. A concept is also presented of using ultrasound to improve the heat transfer between two different mediums in a membrane heat exchanger. As stated by GONDREXON *et al.* (2010), the application of ultrasound can produce a 2.5 increase in the heat transfer coefficient.

Experimental studies of the synthetic jet impact on intensification of the heat transfer generated by a heated plate are presented by CHAUDHARI *et al.* (2010). A synthetic jet is formed if a fluid is periodically sucked into and discharged from a properly shaped cavity due to the motion of a diaphragm. By directing the produced jet to a specific location, the heat transfer conditions can be intensified even though there is no inflow of fresh air into the system under consideration. The investigations prove that the efficiency of this type of cooling at identical boundary conditions is similar, and in some cases even better, compared to continuous cooling by means of an air jet.

Studies of the impact of an oscillating wall on free convection intensification in a criss-cross channel with heated walls are discussed by FLORIO and HARNOY (2011). The obtained results indicate that such a solution leads to an about 30% rise in the mean value of the heat transfer coefficient compared to the situation with no movable elements. The application of the methods described above is to a certain degree limited by the need to use powered movable elements. The success of the application is also strongly dependent on the limited reliability of the solutions due to the fatigue strength of the materials used to make the movable elements, which poses another difficulty.

This paper also investigates a case where an acoustic wave is used for the heat transfer intensification. However, the acoustic wave is generated using a properly shaped immovable cavity placed in the flowing fluid. This solution has a number of advantages, the most important of which are reliability and simplicity of implementation.

Preliminary results of studies on the use of a cavity as an acoustic wave generator for the purposes of the heat transfer intensification are presented by RULIK *et al.* (2015). They concern the possibility of improving cooling conditions in regions of the coolant stagnation. The analysed case is similar to a U-type channel used in convective cooling of the gas turbine blades (WANG *et al.*, 2015). The analyses conducted in this paper draw on and supplement the research presented by RULIK *et al.* (2015). However, a different geometry of the cavity is considered here and a different numerical model is applied. The introduced modifications result from the need to adapt the numerical model to data available in literature. The flow conditions are investigated in a wide range and the obtained

results are compared to empirical relations and correlations.

The analysis of the acoustic wave generation and of the wave impact on the heat transfer intensification is divided into two main stages. The aim of the first part of the studies is to determine the free flow optimal velocities for which considerable pressure pulsations are obtained in the cavity area. At this stage, the impact of the pressure pulsation on the heat transfer in the cavity is not analysed directly, and attention is focused on the selection of cases for further analysis taking account of the heat transfer in the cavity area. Such an approach is imposed by the immensely time-consuming character of the calculations needed to be performed, especially in the case of analysing the heat transfer in the cavity.

2. Mechanism of sound generation in the cavity

If a cavity is filled with gas, it can act as an acoustic resonator. The force that produces acoustic oscillations in this case is the turbulence created in the cavity neck area. The turbulence is an effect of the air jet separation at the cavity leading edge. The oscillations can also be induced by a force related to the feedback mechanism described by ROSSITER (1964) and discussed by ÜNALMIS *et al.* (2004), or due to passive excitation by the pressure fluctuations that may arise in a turbulent flow. The mechanism is also known as the turbulent rumble (DE JONG, BIJL, 2010).

The theoretical model presented by Rossiter makes it possible to determine the frequency of the pressure oscillations inside the cavity. It is based on the assumption that there is a feedback mechanism between the frequency of the generation of vortices in the open narrowing of the cavity and the emitted acoustic wave. The acoustic wave arises due to an impulse generated by the vortices impacting on the cavity rear wall. The process is presented schematically in Fig. 1.
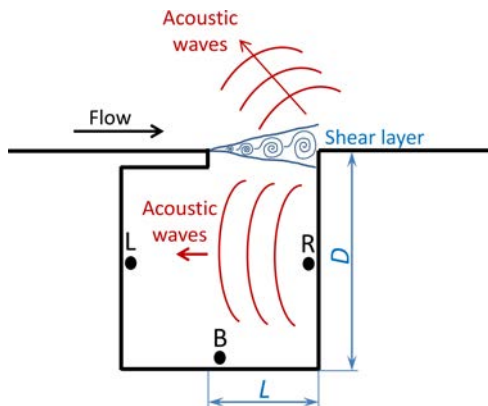

Fig. 1. Feedback mechanism (RULIK *et al.*, 2010).

Some of the acoustic waves are released beyond the cavity, but the rest of them move inside in the direction

opposite to the fluid flow and, thereby, force the flow of new vortices. Consequently, the frequency of the vortices flow in the cavity open neck should correspond to that of the generated acoustic wave. This can be expressed using the following relation (ÜNALMIS *et al.*, 2004):

$$f = \frac{k u_\infty}{\lambda_v} = \frac{c}{\lambda_a}, \tag{1}$$

where k is the ratio between the vortex convection velocity and the free flow velocity u_∞, λ_v and λ_a are the wave lengths directly related to the flow of vortices in the cavity neck area and to the generated acoustic wave, respectively.

Rossiter combined in his model the two mechanisms by introducing quantity α which informs about the phase shift between the moment of the vortex impact on the cavity rear wall and the moment of the acoustic wave generation. The two quantities are usually selected empirically. The values of k and α are typically included in the range of 0.5–0.75 and 0–0.25, respectively (ÜNALMIS *et al.*, 2004). According to Rossiter the Strouhal number can be defined as:

$$\mathrm{St} = \frac{fL}{U_\infty} = \frac{m - \alpha}{\mathrm{M} + \frac{1}{k}}, \qquad m = 1, 2, 3. \tag{2}$$

Another mechanism of the acoustic wave generation mentioned above is the turbulent rumble. In this case, the resonance frequency of the generated acoustic wave should be independent of the free flow velocity (DE JONG, BIJL, 2010). The cavity can then act as the Helmholtz resonator, or a number of standing waves can occur between the cavity walls due to interference of the generated free-travelling waves.

The first type of the resonance occurs at relatively low Mach numbers ($\mathrm{M} < 0.2$), especially for deep overhang cavities ($L/D < 2$). The other resonance type usually occurs in the case of supersonic flows.

The frequency of the acoustic wave produced by the Helmholtz resonator can be described using the following relation (SINGH, NIKAM, 2009):

$$f = \frac{c}{2\pi} \sqrt{\frac{A}{V Z_{\mathrm{eff}}}}. \tag{3}$$

The cavity effective height Z_{eff} depends on the geometric height of the cavity neck Z and the neck geometry (DE JONG, BIJL, 2010).

In the case of the Helmholtz resonator, the air column in the cavity is subject to periodic compression and expansion, which is related to compressibility of air as such. For cavities with leading edge overhang, the pressure pulsations arising from the feedback mechanism and the pulsations resulting from the effect of the cavity acting as the Helmholtz resonator can occur simultaneously, which intensifies oscillations (LOH, 2004).

Considering the second resonance type, the frequency of the arising standing waves can be determined using the following formula (DE JONG, BIJL, 2010; SODERMAN, 1990):

$$f_c = \frac{c}{2}\sqrt{\left(\frac{m_x}{L}\right)^2 + \left(\frac{m_y}{D}\right)^2 + \left(\frac{m_z}{W}\right)^2}. \qquad (4)$$

For small velocity values (M < 0.2), a vertical standing wave can be created between the cavity wall and the cavity open inlet, where a vortex path is formed. The frequency of the generated acoustic wave can then be described using the following relation (JONES *et al.*, 2010; WITTICH *et al.*, 2011):

$$\frac{fD}{c} = \frac{0.25}{1 + 0.65\left(\frac{L}{D}\right)^{0.75}}, \qquad L/D \le 2. \qquad (5)$$

This relation, expressed with the dimensionless Strouhal number, can be expressed as follows (JONES *et al.*, 2010; WITTICH *et al.*, 2011):

$$\frac{fL}{u_\infty} = \frac{0.25\left(\frac{L}{D}\right)}{M\left[1 + 0.65\left(\frac{L}{D}\right)^{0.75}\right]}, \qquad L/D \le 2. \qquad (6)$$

In the case of a cavity with a leading edge overhang, the characteristic dimension is the cavity neck width L.

3. Numerical model

The presented calculations are performed using the Ansys CFX 16.0 commercial CFD code. The applied software uses an implicit finite volume formulation to construct discretised equations representing the Unsteady Reynolds-Averaged Navier-Stokes (URANS) equations for the compressible fluid flow (RULIK *et al.*, 2011; SHAHI *et al.*, 2014). The basic set of balance equations takes account of the continuity, momentum, and energy transport equations:

$$\frac{\partial \rho}{\partial t} + \nabla \cdot (\rho \mathbf{U}) = 0, \qquad (7)$$

$$\frac{\partial(\rho \mathbf{U})}{\partial t} + \nabla \cdot (\rho \mathbf{U} \otimes \mathbf{U}) = -\nabla p + \nabla \cdot \boldsymbol{\tau}, \qquad (8)$$

$$\frac{\partial(\rho h_{\text{tot}})}{\partial t} - \frac{\partial p}{\partial t} + \nabla \cdot (\rho \mathbf{U} h_{\text{tot}}) = \nabla \cdot (\lambda \nabla \mathrm{T})$$
$$+ \nabla \cdot (\mathbf{U} \cdot \boldsymbol{\tau}). \qquad (9)$$

The stress tensor τ is related to the strain rate by means of the following expression:

$$\boldsymbol{\tau} = \mu_{\text{eff}}\left(\nabla \otimes \mathbf{U} + \mathbf{U} \otimes \nabla - \frac{2}{3}\mathbf{I}\nabla \cdot \mathbf{U}\right). \qquad (10)$$

The total h_{tot} enthalpy is related to static enthalpy h in the following way:

$$h_{\text{tot}} = h + \frac{1}{2}\mathbf{U}^2. \qquad (11)$$

The term $\nabla \cdot (\mathbf{U} \cdot \boldsymbol{\tau})$ in Eq. (9) represents the work due to viscous stresses and is called the viscous work term.

Turbulence is modelled using the two-equation Shear Stress Transport (SST) turbulence model proposed by MENTER (1993; 1994). It is a combination of two turbulence models, thus combining the advantages of the Wilcox k-ω model near the wall and the standard k-ε model in what is referred to as the far field.

The model is based on the turbulent viscosity definition expressed by the following relation:

$$\mu_{\text{eff}} = \mu + \mu_t. \qquad (12)$$

In the turbulence model, turbulent eddy viscosity is computed from turbulent kinetic energy k_e and turbulent frequency ω:

$$\mu_t = \rho \frac{k_e}{\omega}. \qquad (13)$$

The analysed computational area is presented in Fig. 2. It is a 40 mm-high flow channel with a single cavity located along it. The cavity is partially covered in the inlet area and its depth is characterised by the L_1/D_2 ratio of 0.56. The cavity dimensions are twice bigger compared to the experimental studies conducted by HENDERSON (2000), with the L/D ratio kept constant. This will make it possible to determine the scale effect on the acoustic oscillation amplitude and frequency. The cavity is located in the middle of the channel, and the channel length equals 40 D_1. The thickness of the computational domain is only 1 mm. For this reason, the conducted CFD analysis should be treated as a two-dimensional one.
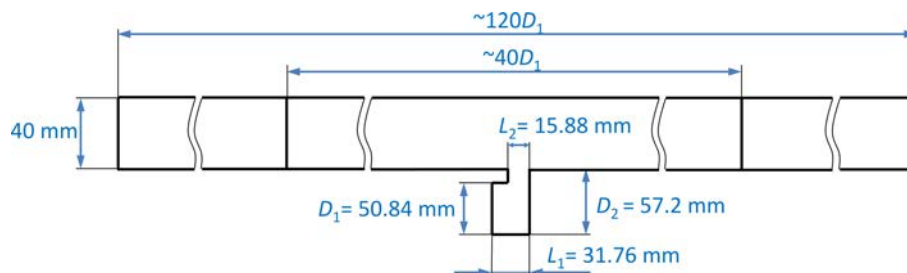
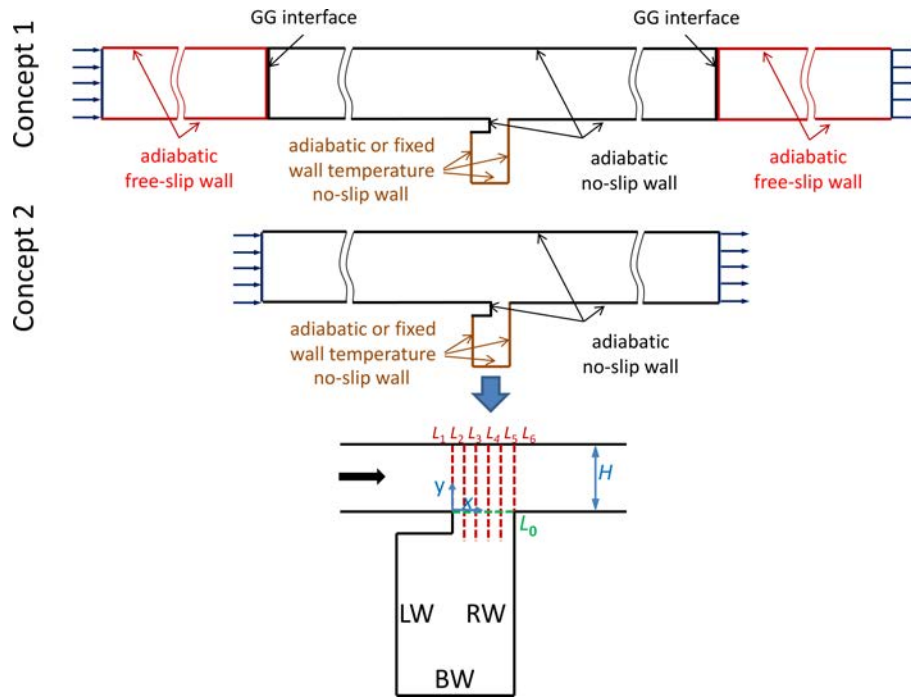Fig. 2. Computational area adopted for the analysis.

Fig. 3. Variants of boundary conditions assumed for the CFD analysis.

The adopted boundary conditions are illustrated in Fig. 3. The symmetry boundary condition is assumed for the channel lateral walls, and the no-slip boundary condition is adopted for the bottom and the top surface. It should be emphasised that two different concepts are used during the calculations to eliminate the acoustic wave reflection from the edge of the computational domain. One of them consists of using no-reflection boundary conditions. The concept may be unreliable for high-amplitude waves and drawing on it may cause the computational process instability. For this reason, another concept is put forward, which involves using additional domain at the inlet and outlet with a relatively thin mesh, where acoustic waves are dissipated before they reach the edge of the computational area. However, this solution requires a higher number of computational nodes.

The additional domain is connected to the flow channel using the General Grid Interface. In the additional area, the free-slip boundary condition is assumed for the bottom and top walls. As a result, the area does not cause additional losses that could arise in the flow channel due to friction. The two variants of the computational domain were compared and the results of the comparison are very similar. This solution ensures greater stability for all boundary conditions under consideration.

The applied numerical mesh is presented in Fig. 4. It is a structural, orthogonal mesh with 231 thousand nodes. Due to the assumed symmetry of the flow, the computational domain span is discretised using a single element, which corresponds to a two-dimensional
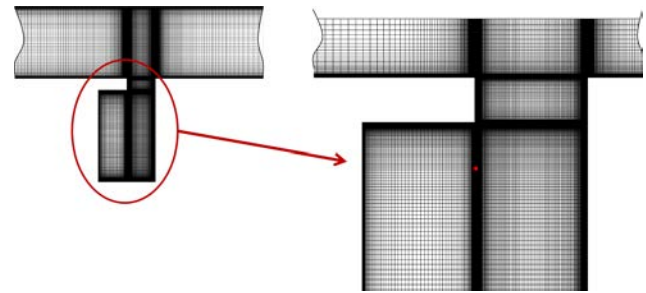

Fig. 4. Detail of the numerical mesh adopted for the CFD analysis.

flow analysis. The numerical mesh is much denser in the cavity neck area. For all walls of both the channel and the cavity, the non-dimensional value $y^+ \approx 1$. The mesh density decreases gradually in the channel inlet and outlet directions. In the interface area, a step change occurs in the size of the numerical mesh elements. At the same time, the mesh density is not increased in the additional domain along the channel edge due to the assumed boundary condition of a free-slip wall. The basic boundary conditions and the numerical simulation parameters are listed in Table 1.

The size of the applied numerical mesh was selected based on a test covering three numerical meshes with 137, 231, and 581 thousand nodes, respectively. The meshes differed in discretisation, in particular, of the region of the cavity itself and of the cavity neck. In this case, account was taken of the impact of space discretisation on the generated acoustic wave amplitude and frequency in point B (cf. Fig. 1).

Table 1. Boundary conditions and basic assumptions
for the CFD analysis.

Inlet	Velocity: 10–100 m/s Static temperature: 15°C Turbulence intensity: 1%
Outlet	Averaged static pressure: 1 bar
Channel walls	Adiabatic
Cavity walls	Adiabatic or heat transfer with constant wall temperature equal to 120°C
Fluid	Air ideal gas
Heat transfer	Total energy option
Turbulence model	SST

Table 2 presents the impact of space discretisation on the generated acoustic wave amplitude and frequency. Due to the close similarity of the amplitude value between Mesh 2 and Mesh 3, the smaller mesh with 231 thousand nodes was selected for further analysis.

Table 2. Analysis of the impact of space discretisation
on the acoustic wave amplitude.

Mesh	Number of nodes	Amplitude [Pa]	Frequency [Hz]
1	136 650	122.45	1175
2	231 400	173.51	1175
3	581 400	175.09	1175

4. Calculation results

The numerical calculations were performed for two flow models. The first model concerned investigations into the process of noise generation in the cavity. The model is based on the assumption that there is no heat transfer in the case of all walls of both the flow channel and the cavity itself. At that stage of the research, the free flow velocity in the channel over the cavity was considered in a relatively wide range of values: 10–100 m/s. The results were compared to those obtained from empirical formula. After a thorough analysis, a selection was made of the cases adopted for further studies which took account of the heat transfer through the cavity walls.

4.1. Aeroacoustic resonance in a cavity

A numerical analysis of the transient-state flow through a channel with a cavity was conducted for 10 free-flow cases (10–100 m/s with the step of 10 m/s). The course of the solution process was traced based on changes in the flow field values in characteristic points located in the cavity area (points B, L, R shown in Fig. 1). In each case under analysis, the first step was to perform calculations for the steady-state flow model. This provided the initial distribution for the transient flow calculations. For example, Fig. 5 and Fig. 6 present the curves illustrating gauge pressure oscillations in points B, L, and R up to the moment of stabilisation of a specific amplitude of acoustic oscillations for the velocity of 50 and 80 m/s, respectively.

The time step of 10^{-5} s was assumed for the simulation of the transient-state flow. At the velocity of 50 m/s, there were 87 time steps per one period of the acoustic wave generated by the cavity. In order to ensure an appropriate number of points to discretise changes in parameters over time for cases with the free flow velocity higher than 60 m/s, calculations were performed for the time step of $2.5 \cdot 10^{-6}$ s. At the free flow velocity of 80 m/s, this gave 110 time steps per one period of the acoustic wave. The calculations made with increased time discretisation produced a rise in the acoustic oscillation amplitude by 8% and 14% for the free flow velocity of 70 m/s and 80 m/s, respectively. It is worth mentioning that for the velocity of 90 m/s, significant acoustic oscillations with an amplitude of about 650 Pa were captured only at improved
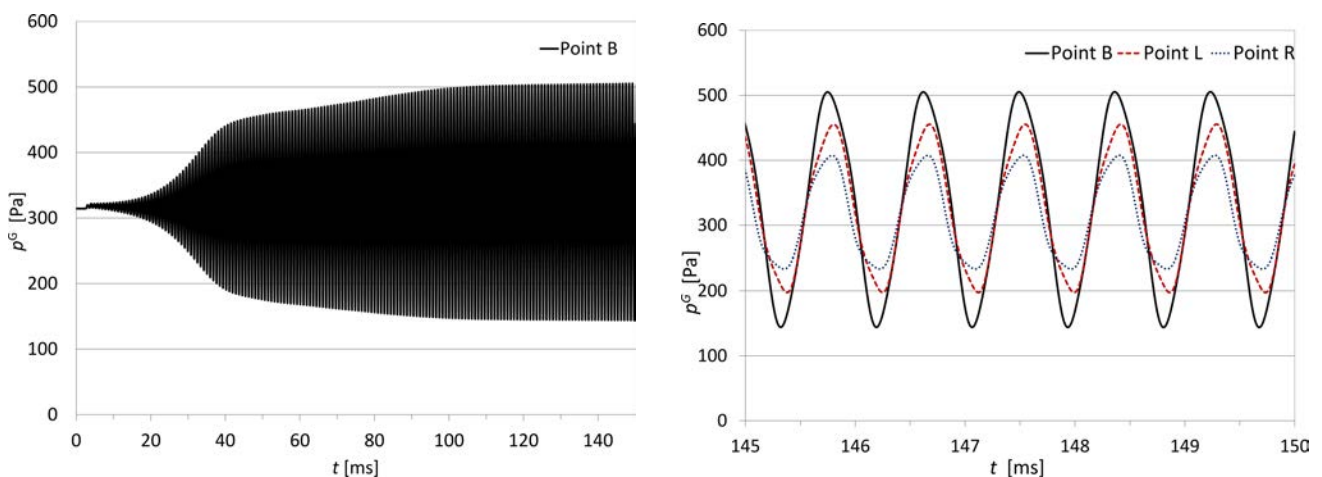

Fig. 5. Gauge pressure fluctuations at the channel flow velocity of 50 m/s.
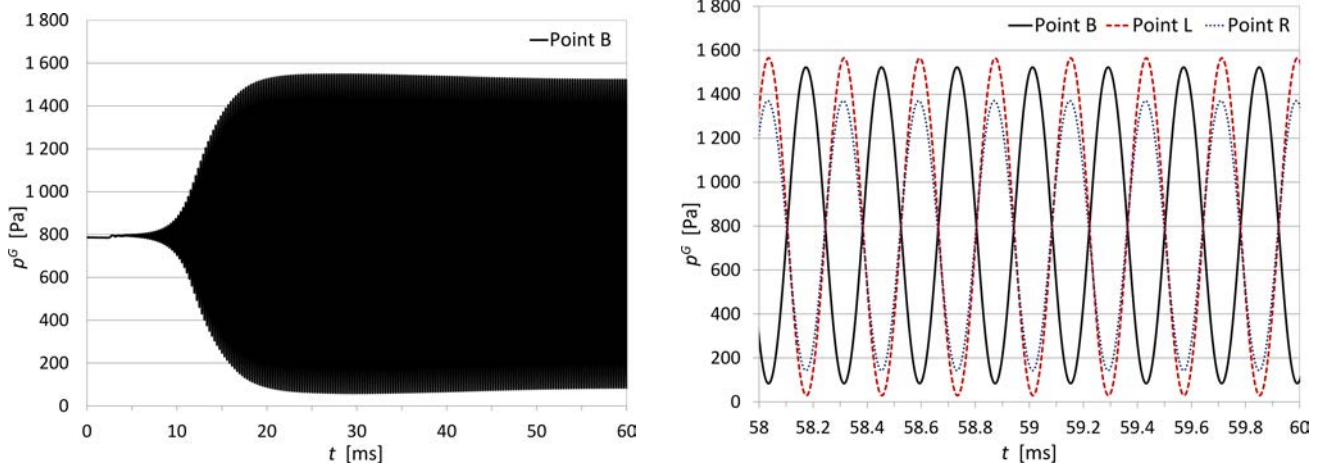
Fig. 6. Gauge pressure fluctuations at the channel flow velocity of 80 m/s.

time discretisation, whereas for the basic time step of 10^{-5} s they were negligibly small.

Depending on the adopted time discretisation and the assumed free flow velocity, the process of stabilisation of a specific amplitude of the generated acoustic wave required 5000 to 24 000 computational iterations.

The charts show that the process of stabilisation of a specific amplitude of oscillations depends on the adopted flow velocity value. However, it is justified to say that, considering the other velocity values under analysis, the higher the oscillation amplitude, the faster the process of the amplitude stabilisation at a specific level. The pressure history analysis performed for three measuring points located in the centre of each of the cavity walls (points B, L, and R in Fig. 1) indicates that for both values of the flow velocity the curve illustrating changes in pressure is close to sinusoidal. However, it should be noted that in the case of the velocity of 50 m/s, the course of the oscillations is characterised by phase coincidence for all the measuring points. Additionally, in the case of points located on the left (point L) and on the right (point R) side of the cavity, the pressure curve is deformed slightly. In the case of the velocity of 80 m/s, pressure on the cavity bottom (point B) is in the opposite phase compared to points L and R. Moreover, for all the points under analysis the pressure change curve is almost sinusoidal. However, the oscillation phase for the velocity of 50 m/s suggests that we are dealing here with the work of a cavity corresponding to the Helmholtz resonator. It is pointed out (LOH, 2004) that the Helmholtz resonance and the feedback mechanism described by ROSSITER (1964) may occur simultaneously. It seems that such a mechanism occurs here, which can also account for the slight deformations of the sinusoidal pressure curve for point L and point R. In the case under consideration, it is impossible to use relation (2) directly to determine the Helmholtz resonator oscillation frequency due to

the two-dimensional character of the conducted numerical analysis. The classical feedback mechanism described by Rossiter can be seen for the flow velocity of 80 m/s. Longitudinal pressure waves occur in this case, intensifying and forcing a specific frequency of the flow of vortices from the cavity leading edge. It should be noted that formula (2), which describes the mechanism, gives good agreement with experimental studies for M > 0.2 (ROSSITER, 1964).

Figure 7 presents the acoustic oscillation spectrum for point D, located in the centre of the cavity bottom wall, depending on the Strouhal number. In this case, the dimension characteristic for the Strouhal number is the cavity neck width L_2 (cf. Fig. 2). No significant acoustic oscillations were obtained for the velocity of 10, 20, or 60 m/s, and therefore the results for these values are not shown in the charts. A linear increase in the acoustic oscillation amplitude can be noticed in the velocity range of 30–50 m/s and frequency values rise from the value of 40 to 174 Pa. The acoustic oscillation frequency obtained for these velocities is included in the range of 780–1150 Hz, which corresponds to the Strouhal number of 0.41–0.36. For the velocity range of 70–90 m/s, there is an abrupt change in the obtained acoustic oscillation frequency, compared to the velocity values of 30–50 m/s. The oscillation frequency for this velocity range is similar and totals from 3420 to 3610 Hz. The highest pressure amplitude values of 574 and 647 Pa were obtained for the flow velocity of 80 and 90 m/s, respectively. The calculated values of the Strouhal number at which significant acoustic oscillations occur are included in the ranges 0.35–0.6 and 0.6–0.9 (DURGIN, GRAF, 1992).

Figure 8 presents the time-averaged value of the convection velocity of vortices related to the free flow velocity. It is determined along the horizontal line L_0 shown in Fig. 3. The velocity profiles determined numerically are similar to those obtained experimentally and presented by JONES et al. (2010). According to
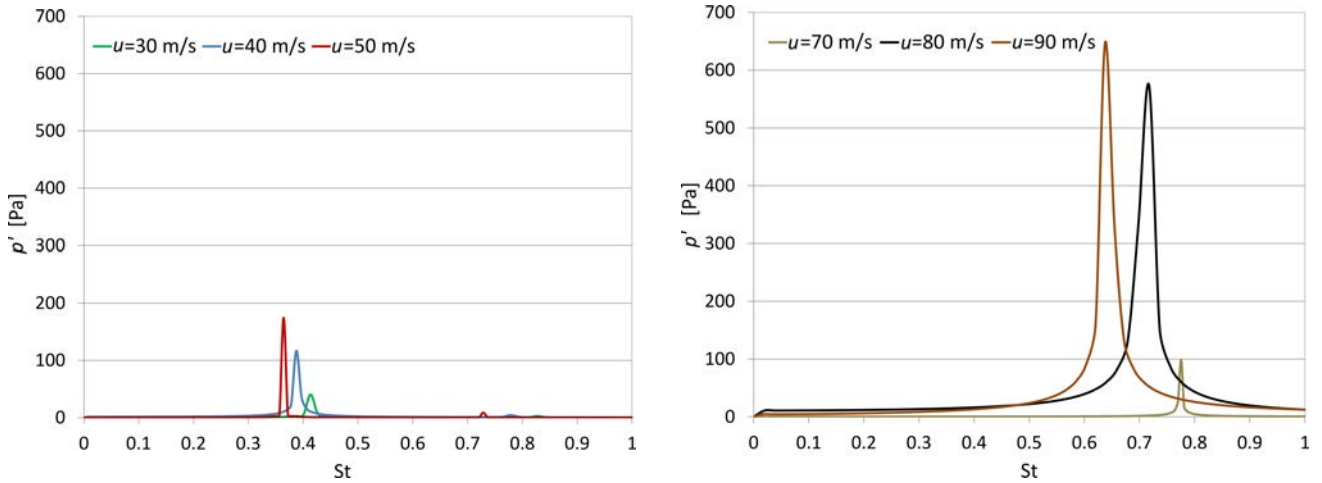
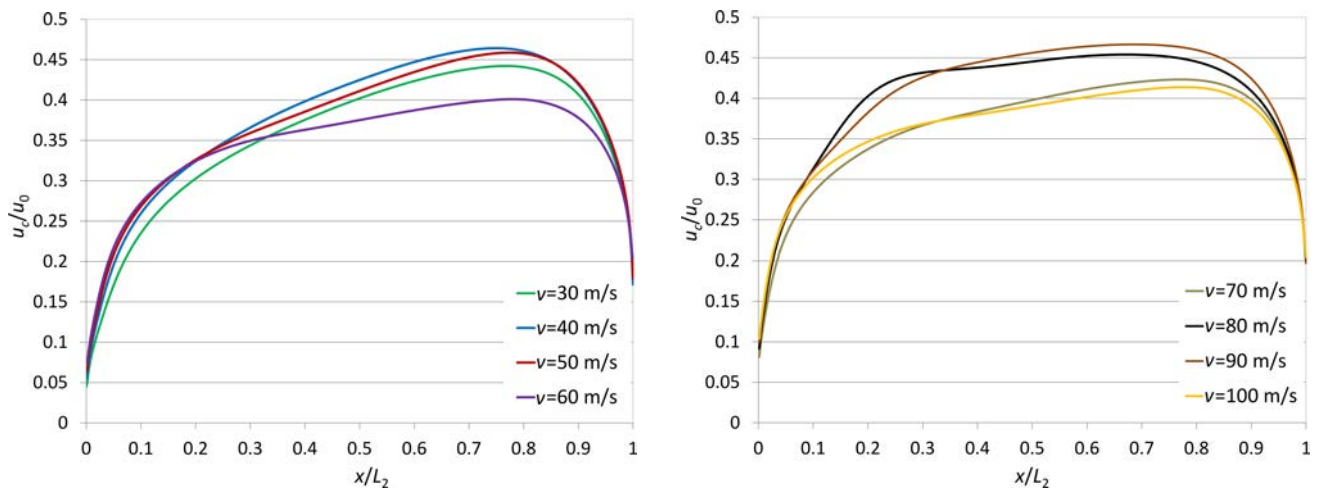Fig. 7. FFT analysis of pressure fluctuations for the free flow velocity of 30–90 m/s.

Fig. 8. Averaged convection velocity depending on the dimensionless width of the cavity neck.

JONES *et al.* (2010) and HASSAN *et al.* (2007), the distribution of the normalised convection velocity value can be divided into four ranges. In the first, convection velocity rises rather abruptly in an almost linear manner. In the second, the velocity increment depending on the cavity width decreases to reach a constant value. Then, in the range of the maximum values, convection velocity is almost constant. Finally, approaching the cavity trailing edge, a drop occurs in the convection velocity value.

It can be seen that for higher values of velocity (exceeding 60 m/s) the curves illustrating the velocity distribution are flattened and, consequently, the range of the occurrence of the convection velocity constant value becomes wider. This is related to the simultaneous more abrupt rise in velocity in the first range in the phase of separation from the cavity leading edge.

Based on the normalised convection velocity characteristics, time scale T_c is determined, which represents the time needed by the vortex structure to cover the entire width of the cavity neck. It is assumed here that the velocity of the vortices is equal to convection velocity in horizontal direction u_{ci}. Time scale T_c is calculated by integrating convection velocity along the cavity neck width, according to the following formula (HASSAN *et al.*, 2007):

$$T_c = \int\limits_0^{L_2} \frac{\mathrm{d}x}{u_{ci}(x)}. \tag{14}$$

The mean velocity of convection is in this case calculated as the ratio between the cavity neck width L_2 and time T_c calculated according to Eq. (14).

Table 3 presents the values of the calculated normalised mean convection velocity for the free flow velocity range of 30–100 m/s. Based on them, the convection velocity mean value was also determined for the entire range of velocities under consideration. The result was 0.374.

Table 3. Values of the normalised mean convection velocity for individual values of the free flow velocity in the channel.

v [m/s]	30	40	50	60	70	80	90	100	
$k = u_{ci}/u_0$	0.357	0.377	0.373	0.346	0.365	0.403	0.408	0.364	$k_{\mathrm{avg}} = \mathbf{0.374}$

Figure 9 presents the Strouhal number value related to the cavity neck width as a function of the Mach number for individual flow velocity values for which a significant acoustic oscillation amplitude was obtained. The value of the generated acoustic wave frequency is determined based on the previous FFT analysis (cf. Fig. 7). The charts present only the fundamental frequency of the generated acoustic wave.

The results obtained from the numerical analysis were compared to empirical relations (2) and (6). For the Rossiter formula (2), in the first variant, the value of the normalised convection velocity k and α are taken as $k = 0.64$ and $\alpha = 0.25$, respectively (cf. Fig. 10a). In the next variant, $k = 0.374$ is assumed as the normalised convection velocity mean value obtained based on the data listed in Table 3. $\alpha = 0$ is assumed in this case as the acoustic delay value, according to HASSAN *et al.* (2007), where it is proved that this assumption often gives better agreement with experimental studies than assuming the value of $\alpha = 0.25$. The comparison shown in Fig. 10b seems to confirm this observation. It can be seen in both charts that the curves obtained from relation (6) generally do not agree with those produced by relation (2). The agreement of the numerical calculation results with the Rossiter formula is better in Fig. 10b. It should also be noted that in this case the agreement occurs also for flows with the Mach numbers lower than 0.2. The numerical analysis produced results which are in better agreement with the charts

obtained based on formula (2). The only exception is the point corresponding to the free flow Mach number $M = 0.15$ (50 m/s). In this case, the numerical calculation results coincide with both the Rossiter formula (2) and relation (6).

Figure 10 presents the distribution of the mean velocity normalised value and the normalised root-mean-square value of fluctuations in the velocity horizontal component in the vortex path generated on the cavity leading edge for six cross-sections L1–L6 shown in Fig. 3. The distributions are presented for three different velocities of the flow: 30 m/s, 50 m/s, and 80 m/s. The calculations indicate that the curves illustrating the distributions of the normalised mean velocity for all the three cases under analysis are very similar. In all cases in cross-sections L2 and L3, in the range of $-0.1 < y/H < 0$, the mean value of velocity was obtained with the direction opposite to the flow main direction. In the cavity neck area, normalised velocity does not exceed the value of 0.2

The history of the RMS values of velocity fluctuations indicates that for the free flow velocity of 30 m/s the fluctuation maximum value occurs within cross-section L3 and totals 0.12. A rise in the flow velocity to 50 m/s involves an increase in the area of high fluctuations in velocity, which then expands to cover cross-sections L3 and L4. The effect of a further rise to 80 m/s is that the highest fluctuations in velocity occur closer to the cavity leading edge and cover cross-section L2 mainly. The contour of the fluc-
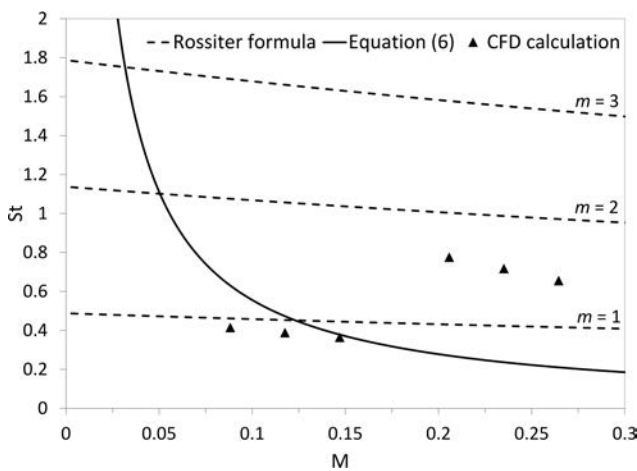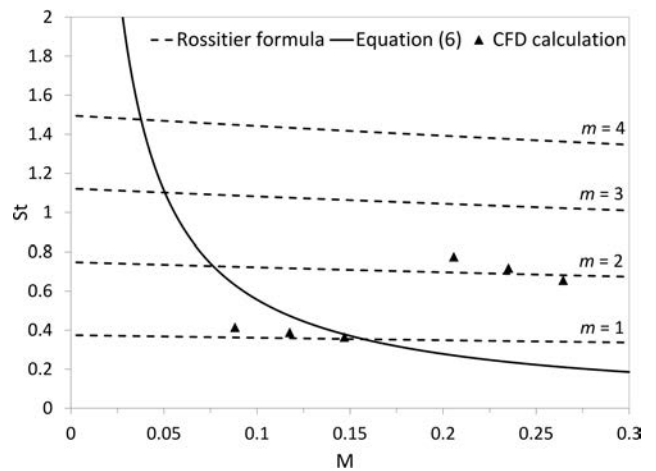
a) $k = u_c/u_0 = 0.65$ and $\alpha = 0.25$

b) $k = u_c/u_0 = 0.374$ and $\alpha = 0$

Fig. 9. Strouhal number depending on the Mach number – comparison between empirical relations and numerical calculations for: a) parameters assumed following by ROSSITER (1964) and WITTICH (2011), b) parameters from calculations and HASSAN *et al.* (2007).
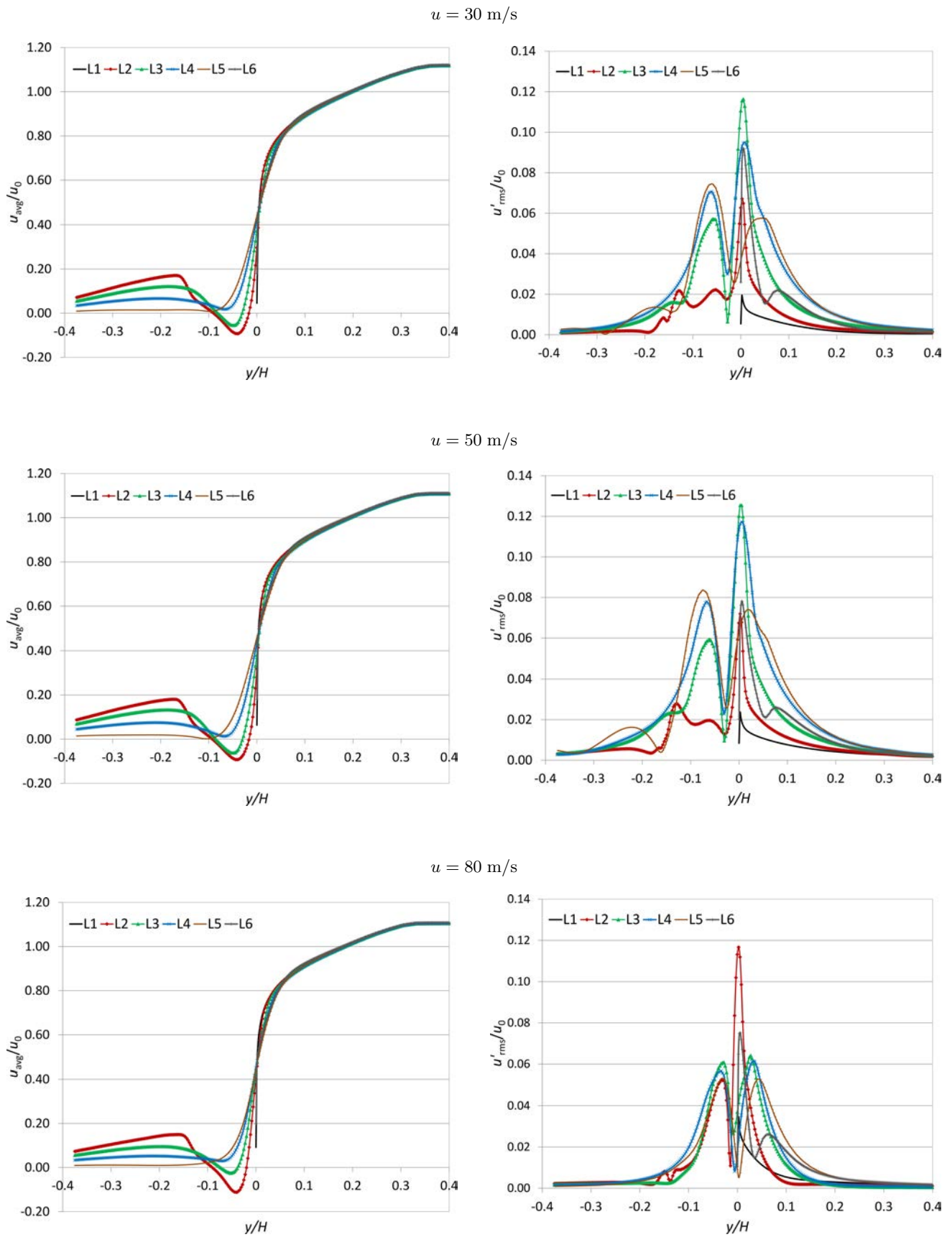
$u = 30$ m/s

$u = 50$ m/s

$u = 80$ m/s

Fig. 10. Value of the flow normalised mean velocity and the RMS value of fluctuations in the velocity horizontal component for the free flow velocity values of $u = 30$, 50 and 80 m/s.

tuation distribution is in all cases characterised by the lack of symmetry relative to line $y/H = 0$ for the cross-section with the maximum value of fluctuations. All distributions occurring upstream the cross-section with the maximum fluctuation in velocity are asymmetrical ones. This asymmetry occurs practically in all cross-sections for the velocity value of 30 m/s. For higher velocities of 50 and 80 m/s, the distributions occurring in cross-sections downstream the one with maximum fluctuations are symmetrical. These changes in shape are characteristic of the formation of the vortex structure. The appearance of symmetry in the velocity distribution proves that a vortex structure has been formed.

The formation of vortex structures in the cavity neck area can be observed in more detail in Figs. 11–14, which present distributions of component z of vorticity. For lower velocity values, a single vortex is generated in the cavity during a single period of the pressure pulsation. For the free flow velocity of 30 m/s and 50 m/s, the vortex is formed in the area of the centre of the cavity neck (cross-sections L3 and L4), and it

is carried towards the cavity trailing edge. For higher velocity values, two vortices are formed in the cavity neck area during a single full period. However, they are generated closer to the cavity leading edge (cross-section L2), and therefore the RMS value of velocity fluctuation reaches its maximum in this point. The velocity of 60 m/s is the transition range, for which the vorticity distribution is shown in Fig. 13. At this velocity, one steady-state vortex is formed below the cavity leading edge. It can stabilise the vortex path direction and development.

It should also be mentioned that the number of vortices generated in the cavity neck area is related to the cavity mode number. According to the experimental work of ELDER *et al.* (1982), the number of generated vortices is equal to the cavity highest oscillation mode. This finds confirmation in Fig. 9, where for the velocity of 70, 80, and 90 m/s the Rossiter formula coincides with numerical calculations for $m = 2$. For the velocity of 30, 40, and 50 m/s on the other hand, good agreement is found for $m = 1$. For all the velocity values analysed herein, a considerable ampli-
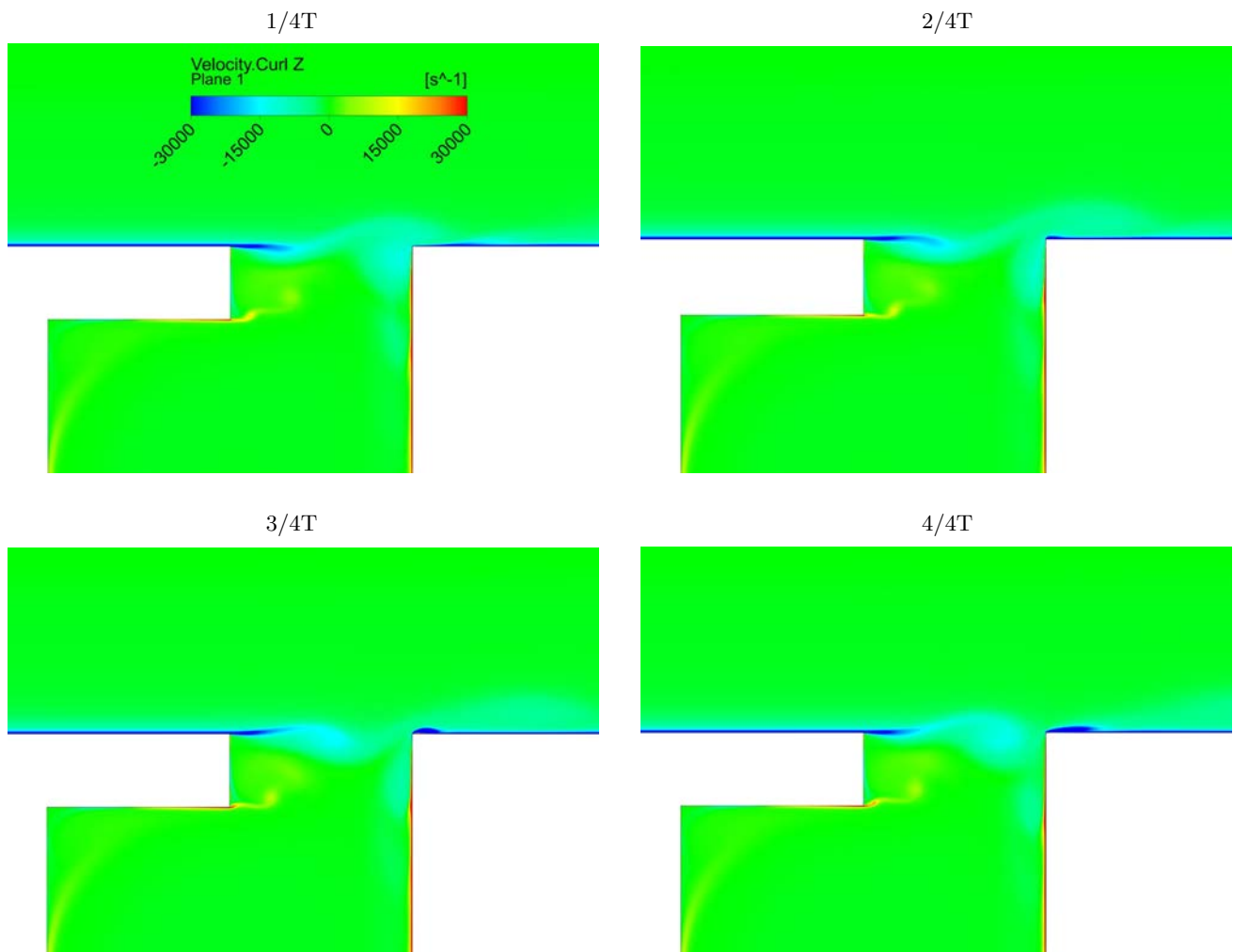

Fig. 11. Distribution of vorticity for the free flow velocity of 30 m/s.

tude was obtained of acoustic oscillations generated by the cavity, except for the transition range, i.e. the velocity of 60 m/s, at which the cavity did not generate significant oscillations in pressure.
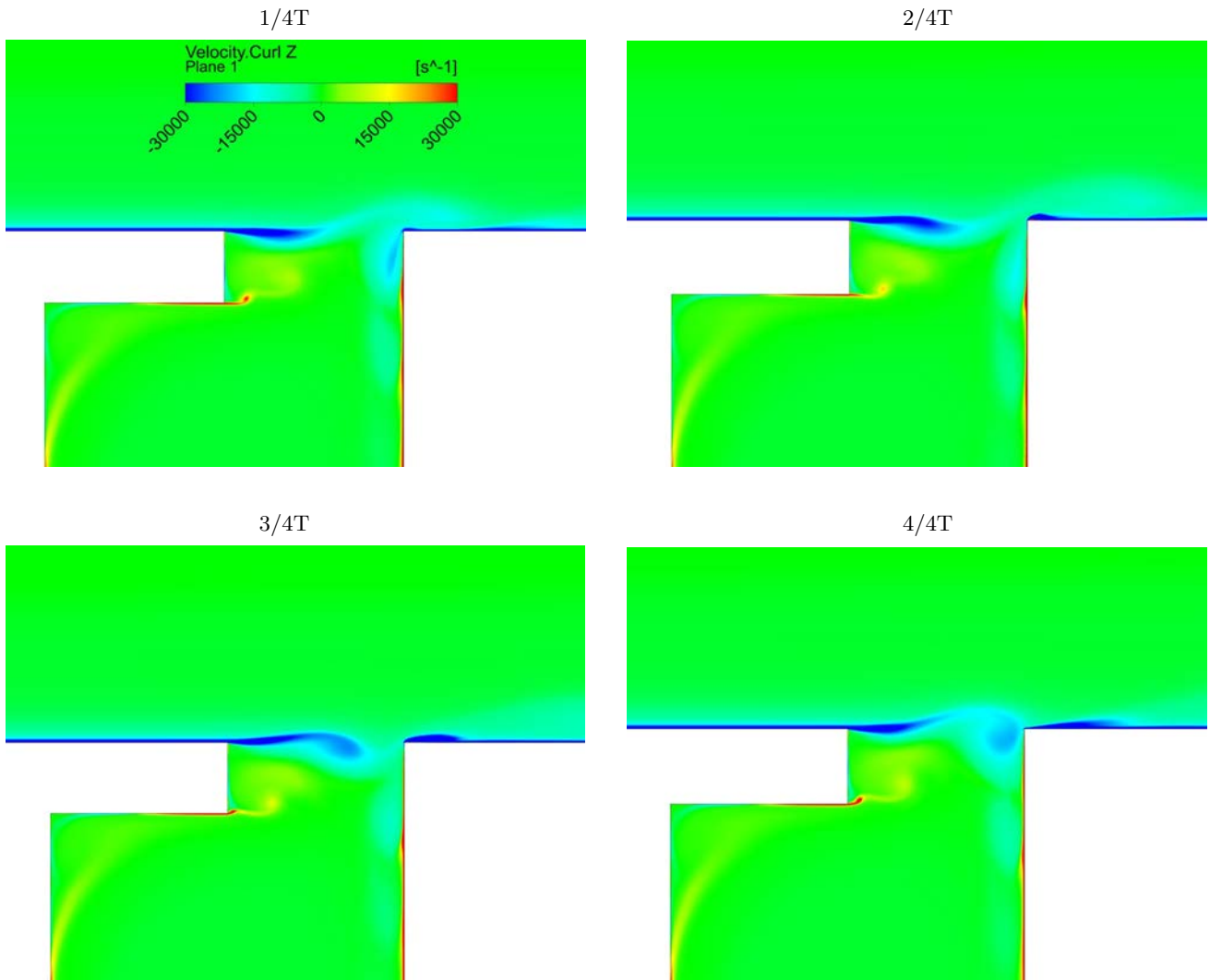

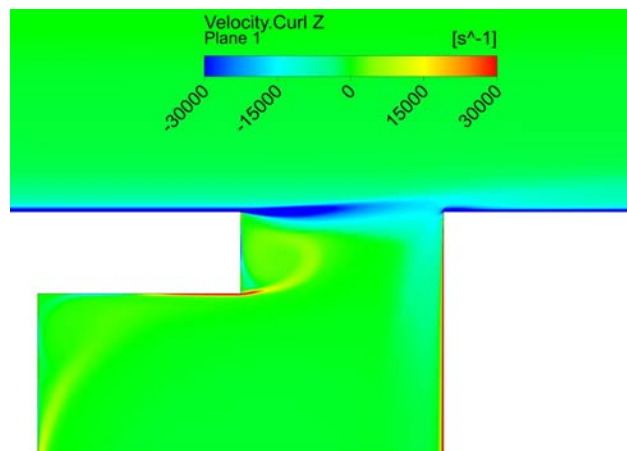Fig. 12. Distribution of vorticity for the free flow velocity of 50 m/s.

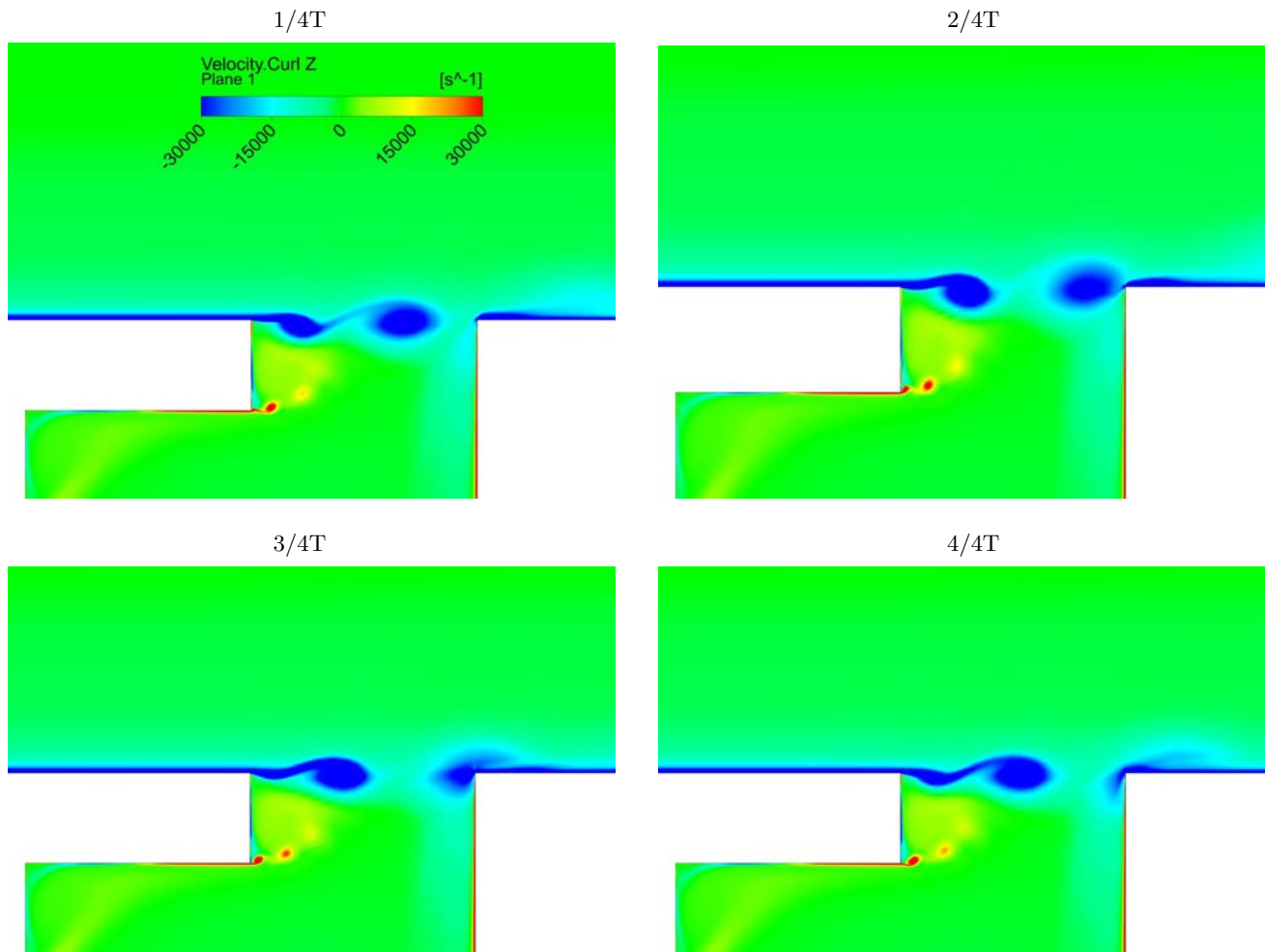Fig. 13. Distribution of vorticity for the free flow velocity of 60 m/s.

1/4T

2/4T

3/4T

4/4T

Fig. 14. Distribution of vorticity for the free flow velocity of 80 m/s.

4.2. Interaction between aeroacoustic resonance in a cavity with the heat transfer

The next stage of the analyses is to determine the impact of flow phenomena in the cavity, as described in the previous section, on the heat transfer conditions. All the numerical analyses were performed for a computational domain with additional domain at the inlet and outlet (cf. Fig. 3 – concept 2) to dissipate all the waves reaching the edge. This made it possible to eliminate the so called no-reflection boundary conditions which often have a negative effect on the computation stability. The modelling boundary conditions of the flow through a cavity are identical to those used in previous analyses (cf. Table 1). The difference concerns the boundary conditions on the cavity walls, where the Dirichlet boundary condition is adopted in the form of the constant temperature of 120°C.

It has to be emphasised that transient heat transfer calculations require a higher number of iterations to obtain stabilisation of a specific temperature distribution in the cavity. In this case, at least 60 thousand iterations were performed for all the variants under

analysis. Like previously, the first stage was to carry out calculations for the steady-state model, and then the obtained distributions of parameters were used as input conditions for the transient-state computations.

Figure 15 presents the temperature field distribution resulting from the calculations made for the free flow velocity values of 50, 60, and 80 m/s. The selected velocities reflect a wide range of flow conditions. They also make it possible to compare the impact of transient-state effects observed at the velocity of 50 m/s and 80 m/s, or of their non-existence at 60 m/s, on the heat transfer conditions in the cavity. Due to a considerable increase in the flow pressure losses, the analysis of the heat transfer conditions for velocities higher than 80 m/s is omitted.

The temperature field obtained based on the steady-state analysis is compared with the time-averaged temperature field resulting from the transient-state computations. A substantial difference can be noticed between the steady- and the unsteady-state solution for the flow velocity of 50 m/s and 80 m/s. In both cases, the transient-state analysis gives much lower temperature values in the cavity. This concerns both
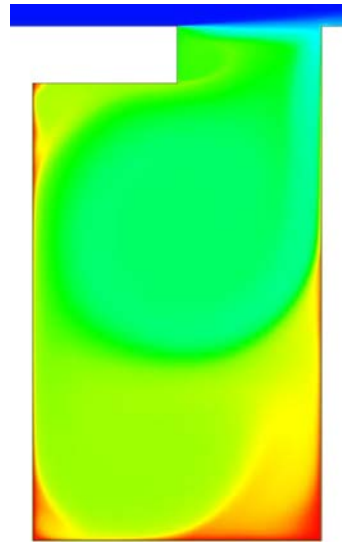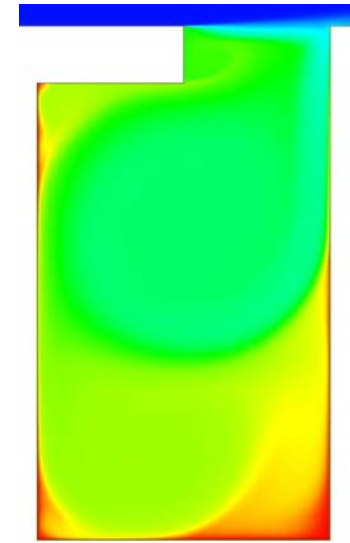
Steady-state analysis, $u = 50$ m/s
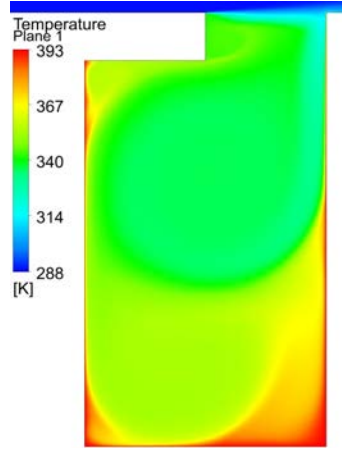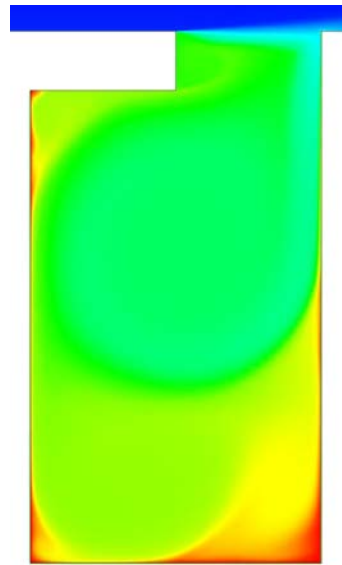
Transient-state analysis, $u = 50$ m/s
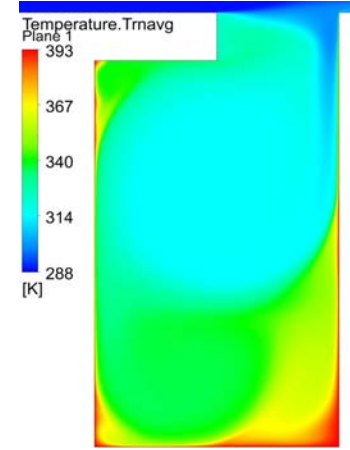
Steady-state analysis, $u = 60$ m/s

Transient-state analysis, $u = 60$ m/s

Steady-state analysis, $u = 80$ m/s
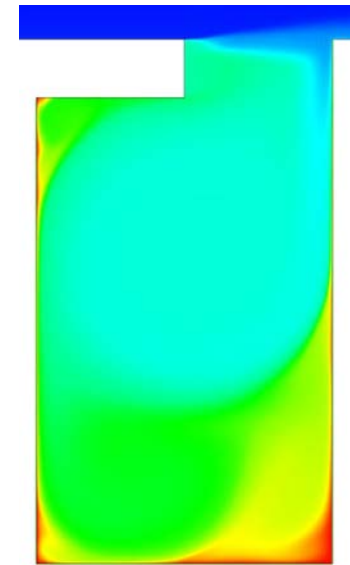
Transient-state analysis, $u = 80$ m/s

Fig. 15. Temperature field distribution in the cavity.

the cavity upper part, with only one noticeable big vortex, and the lower part, where a stagnation region can be observed with much higher temperature values. The difference between the vortex core temperatures obtained in the two simulation types totals about 20 K. A similar difference can be noticed in the cavity lower part. Both simulations performed for the velocity of 60 m/s produced identical temperature fields, which results directly from the fact that there are no significant fluctuations in the flow parameters in the cavity neck area or in the cavity itself. The contours of the temperature field distributions for all the cases under analysis are similar despite the differences concerning the temperature values themselves in the cavity individual regions. This points to a similar nature of the mean velocity field in the cavity area.

In order to assess the heat transfer efficiency, a heat transfer coefficient (HTC) was defined according to relation (15) and relation (16):

$$\text{HTC} = \frac{q}{T_{\text{ad}} - T_{\text{wall}}}, \qquad (15)$$

$$T_{\text{ad}} = \frac{1 + r_c\frac{\kappa-1}{2}M^2}{1 + \frac{\kappa-1}{2}M^2}T_{\text{tot}} \approx T_{\text{tot}}, \qquad (16)$$

where T_{ad} is the wall adiabatic temperature determined from relation (15), and T_{wall} is the wall surface temperature. In relation (16) r_c is the recovery factor, κ is the isentropic exponent, and M is the Mach number. Due to the relatively low velocity of the free flow, it is assumed that the wall adiabatic temperature is the same as the total temperature of the fluid.

The heat transfer coefficient distribution for the cavity individual walls is presented in Fig. 16. In the case of the transient-state analysis, the presented value of the heat transfer coefficient is time-averaged. The obtained results show that the HTC highest value of about 400 W/(m²·K) is achieved on the upper part of the cavity rear wall (RW). The wall is intensely cooled with air impacting on its upper part and then moving gradually downwards. Additionally, some of the vortices generated in the cavity neck flow down with a portion of fresh air and dissipate gradually.

The HTC value then decreases almost linearly to 200 W/(m²·K) for $y/D_2 = 0.1$. The biggest drop in the HTC value is for $y/D_2 > 0.5$. This is related to the stagnation region appearing in the cavity lower part, especially in the cavity corners. The single vortex created in the cavity covers its upper part only, and for this part $y/D_2 < 0.7$.

For the bottom wall (BW), the HTC reaches its lowest value for $x/L > 0.5$, and it is smaller than 1 W/(m²·K). The heat flux maximum calculated value for this wall occurs for $x/L = 0.2$ and totals 5 W/(m²·K). Moderate values of the HTC occur on the cavity left wall (LW). Two local extrema can be distinguished close to $y/D_2 = 0.15$ and $y/D_2 = 0.6$, for which the heat flux density rises substantially. They correspond to the flow structures inside the cavity. A comparison between the steady- and unsteady-state computations shows that there is a considerable difference between the heat transfer conditions for the flow velocity of 50 m/s and 80 m/s. Depending on the location, the difference can be as high as about 70%. For the velocity of 60 m/s the distributions are identical,
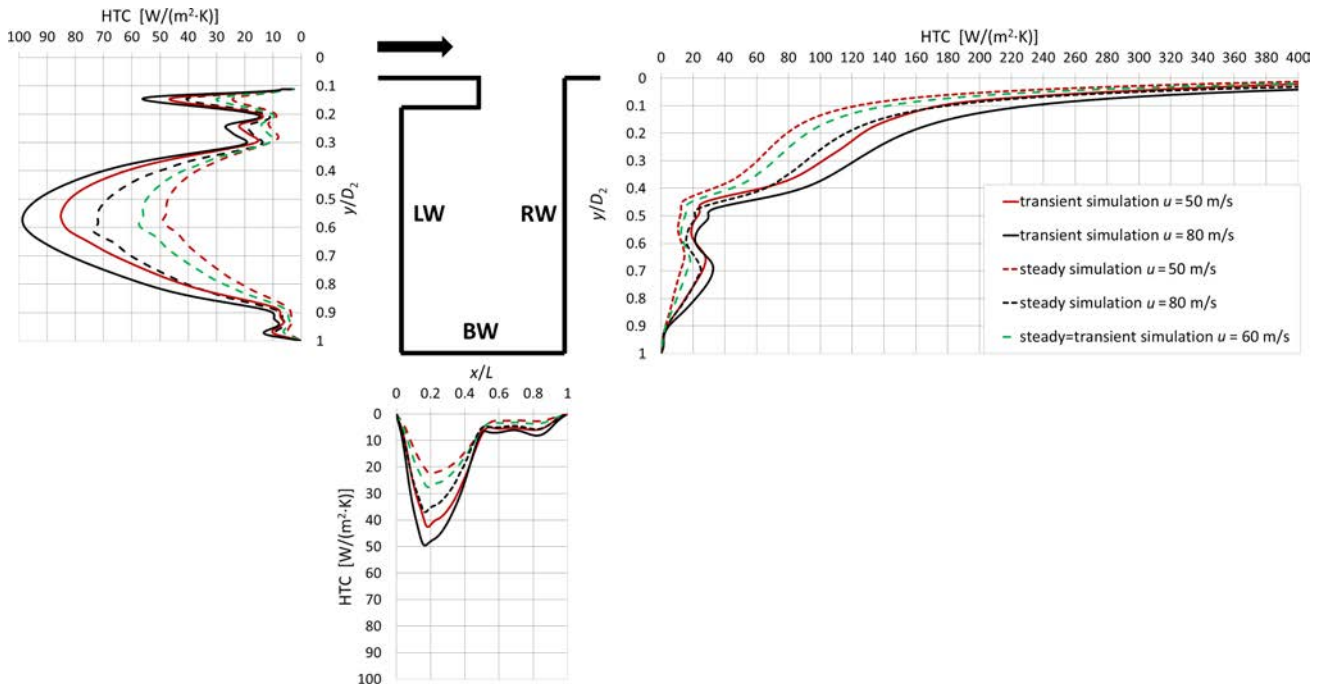

Fig. 16. Heat transfer coefficient distribution along the cavity walls.

which can be already concluded from the identical temperature fields shown previously in Fig. 14. The HTC values obtained for the velocity of 60 m/s are lower compared to those obtained based on the transient-state analysis results at the lower velocity of 50 m/s.

Figure 17 presents the HTC area-averaged mean value for the cavity individual walls. The highest mean HTC values were obtained for the flow velocity of 80 m/s. This concerns all three walls of the cavity. Comparing the free flow velocity variants of 50 m/s and 60 m/s, it can be observed that in the case of the steady-state analysis results, the rise in velocity caused an increase in the HTC value in the range of 17–20%, depending on which wall of the cavity was considered. If the transient-state analysis results are compared, the conclusion is that much higher mean HTC values are obtained for the free flow lower velocity of 50 m/s. For the cavity left wall (LW) and bottom wall (BW), the rise totalled 49.5% and 52.4%, respectively. For the cavity right wall (RW), on the other hand, the increment in the mean HTC value was smaller and totalled 25.5%.
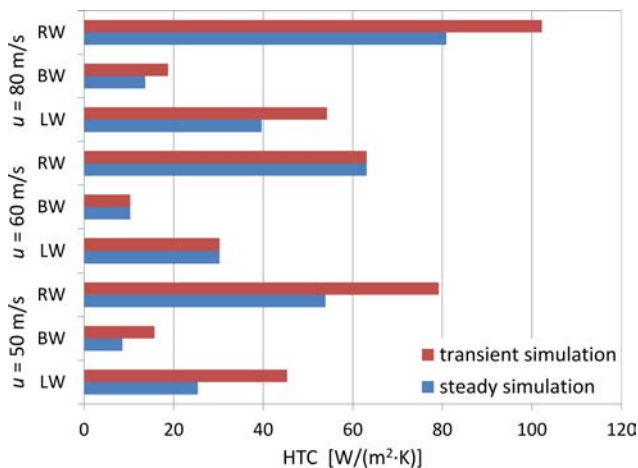

Fig. 17. Mean value of heat transfer coefficient for the cavity walls.

It is also worth mentioning that a 60% rise in velocity from 50 m/s to 80 m/s enables a local increase in the mean HTC value at the level of 19–29%, depending on which cavity wall is taken into consideration.

Achieving a beneficial impact on the heat transfer conditions requires a properly selected value of the flow velocity. If clear non-stationary effects are obtained in the flow due to the acoustic wave generation, a positive impact on the cavity heat transfer conditions can be expected.

5. Summary and conclusions

The works presented in this paper were divided into two stages. The first stage was to analyse only the structure and the process of generating the flow field unsteadiness in the cavity. The obtained results indicate that depending on the free flow velocity taken into consideration, single-phase oscillations can occur in the cavity, or a phase shift is possible between the cavity walls. For the analysed geometry of the cavity and for the free flow velocity range of 30–100 m/s, the obtained mean velocity of the vortex convection along the cavity neck was 0.374. This is substantially different from the value of 0.65, which is usually adopted according to Rossiter (1964) or Wittich *et al.* (2011). The calculated convection velocity made it possible to achieve a significant improvement in the agreement between numerical computations and the Rossiter formula. The best agreement is obtained in this case if the acoustic delay value is assumed as $\alpha = 0$. These conclusions are also in agreement with experimental studies made by Hassan *et al.* (2007). The maximum amplitude of acoustic oscillations is obtained for the velocity range of 80–90 m/s, and it varies between 574 and 647 Pa. For lower velocity values, a single vortex is generated in the cavity neck, whereas for velocities of 70 m/s and higher two vortices are generated during a full oscillation period. The obtained results show that the number of vortices corresponds at the same time to the cavity maximum mode, which is also confirmed by the experimental studies presented by Jones *et al.* (2010) and Hassan *et al.* (2007).

The second stage of the works was to analyse the heat transfer in the cavity and determine the relationship between the heat transfer intensification process and the parameters of the generated acoustic wave. It is found that if the generated acoustic wave is characterised by a high amplitude, the heat transfer coefficient distributions for the steady-state and the transient-state solution differ substantially. The lowest HTC values are obtained for the cavity bottom wall and the highest – for the right wall, where vortices flow after they impact on the cavity trailing edge. This concerns in particular the upper part of the wall, for which $y/D_2 > 0.5$. The analysis of the flow structure inside the cavity and the obtained heat transfer coefficient distribution indicate that the heat transfer can be improved significantly by decreasing the cavity height so that the single vortex generated in it should flow past the bottom wall as well. Further research should focus on the impact of a change in the cavity geometry on the oscillation amplitude of pressure arising inside the cavity, which may additionally improve the heat transfer conditions.

Acknowledgments

fer intensification using an acoustic wave generator", financed by the National Science Centre Poland.

References

1. Ashcroft G.B., Takeda K., Zhang X. (2000), *Computations of self-induced oscillatory flow in an automobile door cavity*, NASA/CP-2000-209790, pp. 355–361.

2. Chaudhari M., Puranik B., Agrawal A. (2010), *Heat transfer characteristics of synthetic jet impingement cooling*, International Journal of Heat Mass Transfer, **53**, 5–6, 1057–1069.

3. De Jong A.T., Bijl H. (2010), *Investigation of higher spanwise Helmholtz resonance modes in slender covered cavities*, The Journal of the Acoustical Society of America, **128**, 4, 1668–1678.

4. Durgin W., Graf H. (1992), *Flow-excited acoustic resonance in a deep cavity: an analytical model*, AMD-Vol. 151/PVP-Vol. 247, Symposium on Flow-Induced Vibration and Noise, Vol. 7, pp. 81–91.

5. Elder S., Farabee T., DeMetz F. (1982), *Mechanisms of flow-excited cavity tones at low Mach number*, The Journal of the Acoustical Society of America, **72**, 2, 532–549.

6. Florio L., Harnoy A. (2011), *Natural convection enhancement by a discrete vibrating plate and a cross-flow opening: a numerical investigation*, Heat Mass Transfer, **47**, 6, 655–677.

7. Gondrexon N., Rousselt Y., Legay M., Boldo P., Le Person S., Bontemps A. (2010), *Intensification of heat transfer process: improvement of shell-and-tube heat exchanger performances by means of ultrasound*, Chemical Engineering and Processing, **49**, 9, 936–942.

8. Hassan M., Labraga L., Keirsbulck L. (2007), *Aeroacoustic oscillations inside large deep cavities*, 16th Australasian Fluid Mechanics Conference, Crown Plaza, Gold Coast, Australia, December 2–7, 2007, pp. 421–428.

9. Henderson B. (2000), *Automobile noise involving feedback-sound generation by low speed cavity flows*, NASA/CP-2000-209790, pp. 95–100.

10. Jones M., Watmuff J., Henbest S. (2010), *Aeroacoustic measurements of a deep cavity in a low-speed flow*, 17th Australasian Fluid Mechanics Conference, Auckland, New Zealand, December 5–9, 2007, pp. 828–832.

11. Léal L. *et al.* (2013), *An overview of heat transfer enhancement methods and new perspectives: focus on active methods using electroactive materials*, International Journal of Heat and Mass Transfer, **61**, 505–524.

12. Legay M., Gondrexon N., Person S.L., Boldo P., Bontemps A. (2011), *Enhancement of heat transfer by ultrasound: review and recent advances*, International Journal of Chemical Engineering, **2011**, article ID 670108.

13. Loh C. (2004), *Computation of low speed cavity noise*, 42nd Aerospace Sciences Meeting and Exhibit, NASA.CR-2004-212892.

14. Loh Ching Y. (2004), *Computation of low speed cavity noise*, NASA/CR-2004-212892.

15. Menter F. (1993), *Zonal two-equation k-ω turbulence model for aerodynamic flows*, NASA-TM-111629, NAS 1.15:111629, AIAA Paper 93-2906, pp. 1993–2906.

16. Menter F. (1994), *Two-equation eddy-viscosity turbulence models for engineering applications*, AIAA-Journal, **32**, 8, 269–289.

17. Rossiter J.E. (1964), *Wind tunnel experiments on the flow over rectangular cavities at subsonic and transonic speeds*, Royal Aircraft Establishment, Technical Report 64037.

18. Rulik S., Wróblewski W., Nowak G., Szwedowicz J. (2015), *Heat transfer intensification using acoustic waves in a cavity*, Energy, **87**, 21–30.

19. Shahi M., Kok. J., Pozarlik A. (2014), *Study of unsteady heat transfer as a key parameter to characterize limit cycle of high amplitude pressure oscillations*, Proceedings of ASME Turbo Expo 2014, Turbine Technical Conference and Exposition, June 16-20, Düsseldorf, Germany, Paper No. GT2014-26311.

20. Singh A., Nikam K. (2009), *Parametric study of wind noise generation from an overhang cavity using morphing technique*, http://www.altairatc.com/india/previous-events/2009/HTC09/FEM_05_Parametric_Study_of_Overhang_Cavity_Acoustics_CRL.pdf.

21. Soderman P. (1990), *Flow-induced resonance of screen-covered cavities*, NASA Technical Paper 3052.

22. Ünalmis Ö., H. Clemens N.T., Dolling D.S. (2004), Cavity Oscillation Mechanisms in High –Speed Flows, AIAA Journal, **42**, 10, 2035–2041.

23. Wang C., Wang L., Sundén B. (2015), *Heat transfer and pressure drop in a smooth and ribbed turn region of a two-pass channel*, Applied Thermal Engineering, **85**, 225–233.

24. Wittich D., Cain A., Jumper E. (2011), *Strong flow-acoustic resonances of rectangular cavities*, International Journal of Aeroacoustics, **10**, 2–3, 277–294.